Local Torrential Rainfall Event within a Mei-Yu Season Mesoscale Convective System: Importance of Back-Building Processes

Honglei Zhang*[1,2,3], Ming Xue*[2], Hangfeng Shen[4], Xiaofan Li[3], Guoqing Zhai[3]

[1]Zhejiang Institute of Meteorological Sciences, Hangzhou, 310017, China

[2]Center for Analysis and Prediction of Storms, and School of Meteorology, University of Oklahoma, Norman, Oklahoma, USA

[3]Department of Atmospheric Science, School of Earth Sciences, Zhejiang University, Hangzhou, 310027, China

[4]Hangzhou Weather Bureau, Hangzhou, 310007, China

Submitted to Advances in Atmospheric Science

February 2023

Revised September 2023

* Corresponding authors: Honglei Zhang, hongleizhang@zju.edu.cn
Ming Xue, mxue@ou.edu

ABSTRACT

An extreme rainfall event occurred over Hangzhou, China during the afternoon hours on 24 June 2013. This event occurred under suitable synoptic conditions and the maximum 4-hour cumulative rainfall amount was over 150 mm. This rainfall event had two major rainbands. One was caused by a quasi-stationary convective line, the other by a back-building convective line related to the interaction of outflow boundary from the first rainband and an existing low-level mesoscale convergence line associated with a Mei-Yu frontal system. The rainfall event lasted 4 hours while the back-building process occurred in 2 hours when the extreme rainfall center formed. So far, few studies have examined the back-building processes in the Mei-Yu season that are caused by the interaction of a mesoscale convergence line and a convective cold pool.

The two rainbands are successfully reproduced by the Weather Research and Forecasting (WRF) model with 4-level two-way interactive nesting. In the model, new cells repeatedly occur at the west side of older cells, and the back-building process occurs in an environment with large CAPE, low LFC and plenty of water vapor. Outflows from older cells enhance the low-level convergence that forces new cells. High precipitation efficiency of the back-building training cells leads to accumulated precipitation of over 150 mm. Sensitivity experiments without evaporation of rainwater show that the convective cold pool plays an important role in the organization of the back-building process in the current extremely precipitation case.

Key words: Torrential rainfall; back-building processes; numerical simulation; trigger

mechanism; convergence line; convective cold pool

https://doi.org/10.1007/s00376-023-3033-6

Article Highlights:

- The genesis of an extreme rainfall and its important back-building process are investigated.
- The cold pool and associated gust front are essential components of back-building MCS.
- Cells along the back-building training line are high precipitation efficiency and low echo centroid.

1. Introduction

Torrential rainfall events can have severe, adverse consequences for society and economy. Government decision making relies on accurate forecasting of such events, which in turn depends to a large extent on the prediction of numerical models. The improvement of numerical prediction requires better understanding of physical processes responsible for the formation and development of extreme rainfall events. Mei-Yu torrential rainfall often occurs along the Yangtze-Huai Rivers basin of eastern China in early summer season. During the Mei-Yu season, southwesterly low-level jet, upper-level trough, subtropical high and the quasi-stationary Mei-Yu front are the mainly weather systems for the production of heavy rainfall (e.g., Tao and Ding 1981; Chen and Yu 1988; Ding 1992). Previous studies reveal that the heavy rainfall during this period is generated by continuous lifting of moist monsoonal air along the Mei-Yu front (Ding and Chan 2005). Many previous studies suggest that extreme rainfall events result from mesoscale convective systems (MCSs), especially from slow moving or quasi-stationary MCSs (e.g., Maddox et al. 1979; Bluestein and Jain 1985; Doswell et al. 1996; Moore et al. 2003). The Mei-Yu rainfall has obviously a quasi-stationary factor, so many Mei-Yu rainfall events have large rainfall accumulation. Some studies show that linear MCSs have greater chances to produce extreme rainfall than nonlinear MCSs (e.g., Houze et al. 1990; Parker and Johnson 2000; Schumacher and Johnson 2005, hereafter SJ2005; Ducrocq et al., 2008). SJ2005 describes two patterns of linear MSCs: “training line-adjoining stratiform (TL/AS)” and “back building/quasi-stationary (BB)”. The back-building process is a pattern when new cells form repeatedly on the upstream side of the old ones and produce stratiform rain downstream. Besides, SJ2005 also suggests that the back-building process is less predictable for the initiation and maintenance of this process because of the nonlinear convective scale processes involved.

For repeatedly formation of new cells in the upstream, a continuous triggering mechanism and continuous supply of instability and moisture are required. Merritt and Fritsch (1984) studied the motion of hundreds of MCSs, and found some cases that were upstreaming moving there were unexplained at that time. Bluestein and Jain (1985) first identified the periodic appearance of new cells upstream that moved into the pre-existing convective line as back-building process. There are many factors for triggering and maintaining back-building MCSs, including orographic lifting (e.g., Barthlott and

Davolio 2016), outflow boundaries (e.g., Doswell et al. 1996; Corfidi 2003; Wang et al. 2014), and frontal zone forcing (e.g., Houston and Wilhelmson 2007, 2012). Among them, one of the most common mechanisms to generate back-building MCS is the forcing by the outflow boundary (or gust front of convective cold pool) produced by older cells. Corfidi (2003) revealed that cold pool played an important role in MCS propagation. SJ2005 noted that some back-building MCSs form and maintain by their own storm-generated outflow boundaries/cold pools. A convective cold pool can lift the low-level air parcel at its leading edge (e.g., Wilson et al. 1998; Ducrocq et al. 2008) or change the low-level circulation locally and enhance convergence areas so as to initiate new cells (Houze 1993; Duffourg et al. 2016; Dahl and Xue 2016). Sometimes, these outflow boundaries will combine with other factors (e.g., cold front, terrain) to produce back-building MCSs. Moore et al. (2012) documented a back-building MCS generated by the interaction of cold front and convectively generated outflow boundaries. Xu et al. (2012) found that a back-building MCS was caused by a cold pool which was trapped by high terrain over Taiwan. The collision of airmasses can also produce back-building MCSs (e.g., Houston and Wilhelmson 2012; Dahl and Xue 2016).

Some studies show that the cold pool lifting mechanism will be impacted by the characteristics of the upstream flow and the environment so as to influence the location and intensity of the convective systems (e.g., Sun et al. 2005; Bresson et al. 2012; Davolio et al. 2016; Li et al. 2021). Duffourg et al. (2018) showed that the environmental moisture structure can influence the development and maintenance of the back-building MCSs. Studies have also found back building processes associated with the Mei-Yu front in the China region (e.g., Wang et al. 2014; Luo et al. 2014; Wang et al. 2016; Wang et al., 2020). The quasi-stationary Mei-Yu front is favorable for the occurrence of heavy rainfall. When it is accompanied by the quasi-stationary or slow-moving back building MCSs, it is easy to produce extreme rainfall. However, few studies have examined the back-building processes that occur during the Mei-Yu season that are caused by the interaction of an existing low-level mesoscale convergence line and the convective cold pool. This is true with the extreme rainfall event to be studied here.

Specifically, the objective of this study is to investigate the back-building processes in an extreme rainfall event (Fig. 1), which occurred over the capital city, Hangzhou, of Zhejiang Province, China. The maximum 4-h accumulative rainfall was over 150 mm. The accumulative rainfall amount during the back-building process which lasted about 2 hours was over 140 mm. According to the climatological study of Zheng et al. (2016), the standard thresholds are divided into three grades according the 70th and 90th percentiles for each of the accumulation periods: Grade I, Grade II and Grade III extreme rainfall. For 3-h extreme rainfall, the thresholds are 125mm and 155mm, respectively. Thus, 3-h rainfall between 125 and 155 mm is defined as Grade Ⅱ extreme rainfall in China, so this case belongs to that category. The event caused massive floods in the northern region of Hangzhou, resulting in significant economic losses including extensive property damages. Zhai et al. (2015) conducted an observational study of this rainfall event, and found that a surface mesoscale convergence line and a meso-γ-scale vortex formed before the occurrence of rainfall event. Their observational study suggested the importance of the vortex in the production of the torrential rainfall. However, the special propagation and organization of the MCS were not studied. The extreme rainfall was mainly caused by the back-building processes, and the propagation direction of the MCS was opposite of the common spread direction of cold pool. To examine more closely the physical processes responsible for the extreme rainfall in this case, in particular the back-building processes in the MCS and their role in producing extreme rainfall, the high-resolution WRF model is used to simulate and analyze this event.

The rest of this paper is organized as follows. Section 2 provides an overview of the extreme rainfall event. Section 3 describes the data used in the numerical model and the design of the simulation experiments. The numerical simulations are validated with the observations in section 4. The results on the back-building processes, the interaction of convective cold pool and a mesoscale convergence line, and the effect of the cold pool, are presented in section 5. A summary and some discussions are given in the concluding section.

2. Case overview

In this section, dense automatic weather station observations provided by the Chinese Meteorological Administration are used for surface analysis and documenting rainfall evolution. Synoptic analysis is presented using the interim European Center for Medium-Range Weather Forecasts Re-Analysis data (ERA-Interim) with a 0.75° resolution (http://apps.ecmwf.int/datasets/data/interim-full-daily/). Radar data from the

Hangzhou Meteorological Bureau are used to document the evolution of the MCS and the back-building processes.

2.1 Rainfall distribution and evolution

The 4-h accumulated rainfall field (Fig. 1a) shows there are mainly two rainbands in this case. One has nearly an east-west orientation (referred to as rainband 1 hereafter) and the other (rainband 2) is located to its southwest and has a northeast-southwest orientation (as marked by the two gray dashed lines in Fig. 1a). Rainband 1 is associated with a quasi-stationary MCS while rainband 2 is related to a back-building MCS that is the focus of this study. The maximum rainfall associated with rainband 2 exceeds 150 mm and the maximum is located near the northeast end of the band (Fig. 1a). To see the time evolution of rainfall associated with the rainbands, 10-min accumulated rainfall at four stations (Tongxiang, Linping, Xingqiao, and Gongchenqiao, marked as TX, LP, XQ, and GCQ in Fig 1a, respectively) are plotted in Fig. 1b. The maximum rainfall of 162.1 mm occurred at GCQ station. Rainband 1 plays an important role in the generation of rainband 2, so the TX station on the western portion of rainband 1 is also plotted. The time series of rainfall (Fig. 1b) show that both the initiation times and the times of maximum accumulated rainfall at the four stations have sequential delays as we move from the northeast most station TX through the southwest most station GCQ, suggesting southwestward propagation of the precipitation systems through the period (from 0740 UTC to 1200 UTC). Rainfall at the three stations along rainband 2 lasts for about 3 hours and shows a primary peak at 0850 UTC for LP and XQ stations and at 0940 UTC for GCQ station, followed by one or two secondary peaks about one hour later (Fig. 1b). The maximum 10-min rainfall at these three stations is between 23 mm and 29 mm. Rainfall starts abruptly and intensifies quickly and reaches peak precipitation in about 30 - 40 minutes.

2.2 Radar analysis

The observed radar reflectivity is used to show the evolution of the rainbands and the back-building processes of rainband 2. At 0700 UTC, in the northeast part of the plotted domain (Fig. 2a) was a line of high reflectivity in the east-northeast to west-southwest direction and it passed through station TX. This line intensified over the next 90 minutes (Fig. 3c) and corresponding the rainfall reached peak intensity at station TX (Fig. 2b). The reflectivity near TX maintained its intensity over the next 40 minutes (Fig. 2e) then moved southeastward and weakened by 1000 UTC (Fig. 2f). This line of convection was responsible for the precipitation along rainband 1 and also played important role in the initiation of convection along rainband 2, as will be discussed later.

Convection along rainband 2 first developed when cell C1 first formed near station LP at 0800 UTC (Fig. 2b). The cell core stayed more or less stationary and intensified over the next 50 minutes (Figs. 2c and 2d) and then started to propagate southeastward and became weaker by 1000 UTC (Fig. 2f). Cell C1 was primarily responsible for the heavy rainfall at stations LP and XQ (Fig. 1) while the secondary peaks at these two stations appeared influenced by cell C2 also as it formed to its southwest and expanded northeastwards (Fig. 2f).

At 0850 UTC, new cell C2 appeared southwest of C1 (Fig. 2d) and became stronger by 0910 UTC (Fig. 2e). It expanded in spatial extent and became linked up with cell C1 to establish a convective line that qualifies as an MCS over the next hour (Fig. 2f). C2 was clearly responsible for most of the precipitation at station GCQ between 0900 and 1100 UTC (Fig. 2 and Fig. 1b). Meanwhile, a third convective cell became established further southwest of C2 (Fig. 2f), and the three cells moved slowly along the connected line northeastwards. The continuous generation of new convective cells upstream of older cells, relative to low-level flow, and the organization of the cells into a southwest-northeast oriented convective line in this case are the typical characteristics of back-building MCSs, and the movement of cells along the line, passing over the same locations, often result in extreme precipitation.

2.3 Synoptic analysis

The geopotential height, equivalent potential temperature, and wind fields at the 1000, 850 and 200 hPa levels are shown in Fig. 3 at 0600 UTC 24 June 2013, or about 2 hours before the heavy rainfall occurred in Hangzhou. At 1000 hPa (Fig. 3a), a cold high-pressure/anti-cyclone system occupied the Bohai Sea, and the subtropical high was located to the south over the northwestern Pacific, while a low-pressure system was located over the Sichuan Basin to the west which extended eastward along a quasi-stationary front. This quasi-stationary front is the Mei-Yu front of this season, which is also a wind shear line with cyclonic flow curvature. The front passed through Hangzhou

City in northern Zhejiang Province. Studies (e.g., Chen and Chang 1980) have found that such horizontal wind shear is often more significant than thermal gradient over southern China for producing precipitation. South of the Mei-Yu front the surface equivalent potential temperature was much higher and south-southwesterly flows brought warm moisture air towards the heavy precipitation region.

At the 850 hPa level (Fig. 3b), the heavy precipitation region was also located within the southwesterly flows that provided low-level moisture in the region (Fig. 3b). At the 200 hPa levels, the precipitation region was located underneath strong west-northwesterly flows at the southern edge of a mid-latitude upper-level jet where anti-cyclonic divergence flows exist (Fig. 3c). The coupling of convergence at the low-levels and divergence at the upper-level provided favorable conditions for convective systems in the region.

2.4 Surface observations

Figure 4 shows analyses of surface temperature and flow fields together with 10-min accumulated precipitation as observed by automated weather stations. At 0700 UTC (Fig. 4a), a mesoscale surface convergence line was clearly evident that passes through the 4 stations discussed earlier. Weak precipitation existed slightly south of the convergence line. According to the synoptic analysis, this mesoscale surface convergence line is a part of the Mei-Yu front. For convenience and consistency, we will use “convergence line” or “near surface convergence line” to describe this part of Mei-Yu front in the ensuing analysis.

By 0810 UTC, rainband 1 has fully developed into a linear MCS, producing significant precipitation and associated surface cold outflow that splits the convergence line (Fig. 4b). The western edge of the cold outflow or gust front reached station LP at 0810 UTC, and 10 minutes later at 0820 UTC, a new precipitation center formed at the station (Fig. 4c) that was associated with cell 1 shown in Fig. 2. By 0910 UTC (Fig. 4d), significant precipitation was found over stations LP, XQ and GCQ, establishing rainband 2 that furthered extends southwestward later via backing building. The surface flows changed to easterly at the location of the original convergence line, due to the southwestward spreading of the outflows along the convergence line.

The above observational results suggest that the cold outflows generated by rainband 1 played significant roles in the initiation of initial cells of rainband 2, while outflows from additional cells on rainband 2 promoted the back-building processes. Still, due to limitation of available data, understanding of the exact processes of outflow-convergence line interaction, the triggering of new cells via back building, and of the production of extreme precipitation requires high-resolution numerical simulations that provide more complete information. The model configuration and simulation results are presented next.

3. Model description

The Advance Research version of the Weather Research and Forecasting Model (WRF-ARW; Skamarock et al., 2007; Klemp et al., 2007) version 3.7.1 is used to simulate this rainfall event. Four two-way nested domains are used (Fig. 5), consisting of grids of 27, 9, 3 and 1 km grid spacings with horizontal mesh sizes of 280 × 220, 301 × 250, 301 × 250, and 202 × 202, respectively. Expect of synoptic scale fields, the model results in this paper are from the inner most domain. The number of vertical level is 57. Since this study focuses on low-level features, 19 levels are configured below 3 km. The model uses the Thompson microphysics scheme (Thompson et al. 2004, 2006, 2008), the rapid radiative transfer model (RRTM) longwave radiation scheme (Mlawer et al. 1997), the Duhdia shortwave radiation scheme (Duhdia 1989), the Mellor-Yamada-Janjic (MYJ) planetary boundary layer scheme (Janjic 1994), the Noah-MP land surface model and Eta surface layer scheme (Janjic 1996) based on the Monin-Obukhov similarity theory on all domains, while the Grell 3D cumulus scheme (Grell and Devenyi 2002) is used in domains 1 and 2 only. The ERA-Interim reanalyses are used to provide initial and boundary conditions. The simulations are integrated from 0000 to 1200 UTC of June 24, 2013. To examine the impact of cold pool, we performed an additional experiment named NOEVAP, in which cooling from the evaporation of rainwater is removed from the microphysics scheme.

4. Evolution of simulated convection and comparison with observations

We compare synoptic scale fields in the outmost domain with the ERA-Interim data and find that the model reproduces well the large-scale environment before convection occurred in Hangzhou, including the wind shear line extending eastwards from Sichuan Province, the Mei-yu front, the subtropical high over the ocean, and the southwesterly flows on its northwest side at 850 hPa (not shown).

Comparison of the 4-h accumulated rainfall between the simulation (Fig. 6) and the observational data (Fig. 1) show that the model successfully captures two rainbands but their locations are shifted southward and westward by about 20 km (Fig. 6). The maximum accumulated rainfall center of over 140 mm is reproduced, and is located at the intercepting point of the two rainbands. The simulated rainfall also occurs about two hours too earlier. Because of the rainfall in this event is associated with mesoscale convergence line and the Mei-yu frontal system rather than local land surface features, timing and location errors of precipitation often occur due to errors associated with larger-scale features. For our purpose, the most important is that the key physical processes are correctly reproduced in the simulation. Timing and position errors of simulated/predicted mesoscale and convective-scale systems are also encountered in many earlier process studies, such as Weisman et al. (2013) and Xu et al. (2015).

Figure 7 shows the simulated radar composite reflectivity fields, which should be compared to those in Fig. 2. Because the model timing error, the simulated fields shown are 2 h earlier than observations. The model reproduces the nearly west-east-oriented quasi-stationary convective line associated with rainband 1 at 0510 UTC (Fig. 7a) which has increased in intensity and coverage in later hours (Fig. 7). Later, a sequence of new cells forms to the southwest of this line (Fig. 7 b-f), similar to observed (Fig. 2 b-f). To differentiate from observations, we use A, B, C, D to label the simulated cells that form via back building. Cell A is first initiated west of the convection line associated with rainband 1 at 0550 UTC (Fig. 7b). Cell B forms further southwest of cell A by 0610 UTC (Fig. 7c). The two cells reach their maximum intensity by 0710 UTC (Fig. 7e). At 0630 UTC, the gust front from cells B and A is indicated by the thick dashed line in Fig. 7d, while at this time a new cell ahead of the gust front is found along the convergence line. By 0710 UTC, this new cell is fully established and is labeled cell C in Fig. 7e. The formation of cell C is somewhat different from cell C3 in the observation which formed closer to cell C2 (Fig.2) but the process is still physical. Later, cell C merges with cells B and A to form a connected line, and a gust front is found southwest of cell C, and new cells are further triggered at the gust front (Fig. 7f). Overall, the back building processes where new cells are triggered by rearward propagating gust front and eventually organized into a line-oriented MCS are reasonably well reproduced in the simulation, despite certain timing and position errors. In the next section, the cell initiation processes within the model will be examined in more detail.

5. Initiation of convection and production of heavy rainfall

5.1 Cell initiation and development

Figure 8 shows surface features including streamlines, cold pool outflow boundaries, composite reflectivity, convective available potential energy (CAPE), and water vapor mixing ratio at 0540 UTC, about 10 minutes prior to cell A formed (c.f., Fig. 7b). The cold pool boundary is defined where the perturbation potential temperature (θ_e') is -1 K, and θ_e' is defined as departure from the domain-average of θ_e (Dawson et al., 2010). The average domain is the whole domain 4. Figure 8 shows that the arc-shaped convectively generated cold pool is located east of the high CAPE region. The CAPE in the region of interest is over 3200 J kg $^{-1}$. The near surface water vapor mixing ratio (Fig. 8b) in the back-building formation region is over 22 g kg^{-1}.

The level of free convection (LFC) is mostly lower than 600 m, so air parcels can be easily lifted to their LFC, especially in the presence of convergence forcing. Besides, convective inhibition is nearly zero. The large CAPE, weak CIN, and low LFC provide favorable conditions for convective initiations and production of heavy rainfall. The radar reflectivity shows that the storms develop along the convergence line having high CAPE and low LFC. As shown in Fig. 7, this convective line is consisted of cells A – D that are initiated one by one starting from northeast to southwest along the convergence line. As the cold pool expending southwestward, lifting at the gust front and convergence line intercept point initiates new convection.

To see how the environment changes near and upstream of the convection initiation location, skew-T diagrams for soundings extracted from the blue star location in Fig. 8a are shown in Fig. 9. The sounding at 0440UTC (Fig. 9a), which is an hour before the back-building process occurs, shows a moist low-level environment with large CAPE (2927 J kg^{-1}) and low LCL (at 974hPa). The flow is mostly northerly below 1.5km but changes to westerly to southeasterly above. An hour later, the flow below 1.5 km turns to mostly easterly which is mainly caused by the outflow from the rainband 1. The low-level air is still very moist with mixing ratio exceeding 20 g kg^{-1}, and the total precipitable water is 70 mm. The CAPE increases to 2975 J kg^{-1} and LCL becomes lower at 986 hPa, therefore it does not take much lifting for convection to initiate**.**

To see more clearly the initiation process, we plot in Figs. 10 and 11 vertical cross sections across cells A and B through their initiation and development stages (see Fig. 7d for location). As shown in Figs. 3 and 7 (horizontal dBZ), this back-building convective line consists of some discrete echo centers, suggesting a multicell storm. In Figs. 10a and 11a, at 0540 UTC, there is enhanced northeasterly flow (from right to left in the cross sections) near the surface with origination from the convection near the right edge of the cross section (which is part of rainband 1). Clouds have developed with cloud water reaching 1.8 km (Fig. 11a) at the leading edge of the enhanced surface flow or the gust front, with weak reflectivity forming at around 1 km level (Fig. 10a). Vertical velocity is evident at the location of clouds. This is the beginning of cell A.

Over the next 10 minutes by 0550 UTC, the clouds of cell A have reached 2.8 km level (Fig. 11b) while precipitation has reached ground based on the reflectivity (Fig. 10b). The outflow of cell A combined with the old gust front increases the westerly winds near the surface and pushes the surface gust front upstream (in terms of upper-level flow) to the location marked in Fig. 10b. At this time, there is a small blob of cloud water at ~600 m level at the location of gust front, which corresponds to very weak reflectivity at the same location in Fig. 10b. This is the very beginning of cell B. At the location of cell B, the LFC is also very low (Fig. 11b).

Over the next 10 minutes, cell A further develops, with clouds and reflectivity reaching nearly 4 km level (Figs. 10c, 11c), and the cell moves northeastward slightly due to mid-level flow advection. The new cell B upstream of cell A has developed significantly, with clouds and reflectivity reaching 3.7 km level. The gust front has moved further upstream to the left of cell B in the cross section. Over the next 30 minutes by 0630 UTC, the strength of cold pool has increased. The depth of cold pool is now over 1 km. Cell A becomes broader and maintains its echo top height at about 4 km, and becomes connected with convection to its northeast (Figs. 10d and 11d). Cell B has much intensified, and its echo top has reached above 7 km and maximum reflectivity reaches 55 dBZ. Most of the strong echo remains below the freezing level (Fig. 10d), suggesting the precipitation is dominated by warm rain processes, as many heavy-precipitation MCSs in the warm season of China are (e.g., Huang et al. 2019).

Due to the vertical wind shear, the convective cells tilt slightly towards the northeast, and both cells also move slightly towards northeast (Fig. 10). As cells A and B mature, the surface cold pool further spreads upstream (southwestward), and later triggers cell C that forms further upstream (Fig. 7). The processes are similar to the gust-front pulsation mechanism described in Lin et al. (1998), who used an advection mechanism to explain how new cells regenerated at the gust front moved rearwards (relative to the low-level flow) in a multi-cell system. The near surface convergence ahead of the gust front forced an updraft and developed into convective cell in their study. However, the environment conditions in our case are different with those in Lin et al. (1998). In our case, the gust front produced by earlier convective cells propagates upstream (relative to mid-level flows), and triggers new convective cells that subsequently move downstream, and producing heavy precipitation given favorable thermodynamic conditions. This is the typical back building process.

5.2 Precipitation efficiency and water vapor

Because this case produces extreme precipitation rates of more than 20 mm over 10 minutes (c.f., Fig. 1) and most strong echoes are below the 0° isotherm (Fig. 10), how the low top convective cells produce such extreme rainfall is a question worth investigating. How high is the precipitation efficiency of these cells? Huang et al (2014) found that high rainfall rates usually correspond to high precipitation efficiency. Figure 12a shows the precipitation efficiency during the back-building process, following the calculations of Sui et al. (2007) and Huang et al. (2014). They defined the cloud microphysical precipitation efficiency (CMPE) as PE = P/$Cond_T$. P is the time-averaged and volumetrically integrated amount of total precipitation flux. $Cond_T$ is the total condensation and deposition, which can be decomposed into the vapor deposition rates for the growth of cloud ice, snow and graupel, the vapor condensation rate, and the local hydrometeor change and hydrometeor convergence.

To understand the evolution of one cell along the back-building convective line, we focus on cell A and check its precipitation efficiency during its lifetime. For the seldom movement of the cell A from 0540 to 0740 UTC, we choose a 10 km × 10 km region (black box shown in Fig. 7d) to represent the cell A region. The time series of precipitation efficiency (Fig. 12a) shows that at the onset stage of cell A, the precipitation efficiency was about 20 – 40 %. During its mature period, the precipitation efficiency can reach to 80%. From Fig. 7 and Fig10d, cell A does not develop much deeper (below 4 km) but becomes broader and begins to weaken at 0630 UTC. In the meantime, both P and $Cond_T$ have decreased. The decrease in $Cond_T$ is greater than P, thus there is an increase in precipitation efficiency. Though the cells are not very deep, the precipitation efficiency is high enough to produce extreme rainfall. The high CAPE, very high low-level humidity and the presence of mesoscale convergence should also contribute to the extreme rainfall.

The time-height plot of net water vapor flux into the black box shown in Fig. 7d surrounding the cell A region is shown in Fig. 12b. Large inward water vapor fluxes are found below 2 km at 0610 UTC. According to early figures, cell A is in its development stage at this time (Fig. 7c). Negative outward net flux at the low levels starts to appear at 0630 UTC. The main negative flux comes from the west boundary that is close to cell A. From 0630 UTC, cell B develops quickly (Fig. 10d), which might have drawn more air into itself and away from cell A. Development of downdraft in cell A should have also contributed to the negative fluxes. Despite the negative water vapor fluxes at the low levels, large positive fluxes continue to exist between 1 and 2 km levels, and the precipitation efficiency becomes even higher.

5.3 Role of cold pool

To further confirm the role of cold pool in the back building process, we examine the results of experiment NOEVAP, which has the evaporative cooling turned off within the microphysics scheme. Figure 13 shows that the evolution of the simulated radar reflectivity and surface streamlines. The composite reflectivity in panels (b) through (f) of Figure 13 can be directly compared to those in panels (a) through (e) of control experiment in Fig. 7. The quasi-stationary convective line corresponding to rainband 1 is still produced, and it moves southward somewhat away from the surface convergence line later on, but no sequential development of new cells further southwest along the convergence line as in the control experiment. Though previous studies showed that a cold pool is not necessary to organize and maintain convection if large-scale conditions are suitable (Schumacher 2009; Peters and Schumacher 2016), in experiment NOEVAP, the lack of cold pool from earlier convection does influence the later evolution of the convective systems. This was also shown in Jeong et al (2016), which suggested that evaporative cooling leaded to cold outflow that pushed convection progressively toward the oncoming flow. In our case, the lack of cold outflow prevents that the redevelopment of new cells upstream of the gust front via back-building processes.

Figure 14 shows a comparison of surface fields from the control and NOEVAP experiments. At 0510 UTC (Fig. 14a), the control run has produced several areas of precipitation south of the surface convergence line, which expands and becomes a connected line by 0550 UTC (Fig. 14b). Besides, cell A is initiated at the intersectional point of gust front and convergence line (red rectangle in Fig. 14b). This corresponds to observed rainband 1 but with timing and spatial errors (c.f., Fig. 7). In these regions of precipitation, the surface temperature is 3 to 6 degrees colder than warmer regions (Fig. 14b), and the northward spreading of the cold pool has helped to keep the convergence line in place. In contrast, in experiment NOEVAP, precipitation only exists near the northeast end of the convergence line and the surface cold pool is very weak (Figs. 14c, 14d). The convergence line is located further south compared to the control experiment. These results suggest that even for rainband 1, the cold pool plays an important role in convection initiation and organization at the eastern part of the band, and the cold outflow from rainband 1 helps to keep the convergence line stationary. In later hours in the control experiment, the cold pool spreads further upstream and trigger cells A through D (c.f., Fig. 7).

To further analyze the impact of cold pool and the associated back-building process on rainfall, 10-minute rainfall averaged over the pink rectangle region in Fig. 6 for control and NOEVAP experiments are plotted in Fig. 15. The maximum average rainfall rate in experiment NOEVAP is reduced from about 2.4 mm to about 1.35, or by about 44%. The peak in NOEVAP is reached at a slower rate. These results further confirm the critical role of convective cold pools in triggering and supporting new convection, and in producing the extreme rainfall of this case. Cold pool and associated gust front are critical components of the back building process.

6. Summary and conclusions

An extreme rainfall event occurred over Hangzhou, Zhejiang Province, China in the afternoon of 24 June 2013, and produced maximum cumulative rainfall of more than 150 mm in 4 hours. The rainfall was primarily produced by convection organized into two major rainbands and both bands are linked to mesoscale convergence line at the low levels that is part of the Mei-Yu frontal system of the season.

This extreme rainfall case, including the initiation and organization of convection, is studied using radar and surface observations, and output from numerical simulations at 1 km grid spacing (nested within 3 coarser resolution grids). Both the observed and simulated data show the importance of the cold pool and the mesoscale convergence line in producing this torrential rainfall. The extreme rainfall was mainly produced by a sequence of convective cells that developed southwest of the older cells, as the cold pool from the older cells spreads upstream (relative to the middle and upper-level flows) along the mesoscale convergence line and triggers new convection. These cells, after forming, moved very slowly northeastward and producing 10-minute rain rates of over 20 mm over. Such processes are commonly referred to as the back building processes.

A concept model is proposed to summarize the evolution of key processes involved (Fig. 16). A mesoscale convergence line is found between northeasterly flows on the north side and southeasterly flows on the south side. The convergence line is associated with the Mei-Yu front and remains quasi-stationary. At the beginning of this rainfall event, light rainfall forms near the east end of the convergence line and strengthens to become rainband 1 (Fig. 16a). As precipitation of rainband 1 increases, a cold pool due to evaporative cooling is established that spreads mainly westward given the easterly surface flows. The cold pool that tries to spread northward also helps to keep the convergence line in place (Fig. 16b). As the gust front moves westwards and southwestwards, convergence lifting is strongest at the intercepting point of the gust front and convergence line, and the air ahead of the gust front to its southwest has large CAPE, high humidity and low LFC, so it does not take much effort to lift near surface air to its level of free convection, for deep convection to develop. In fact, the cells develop very quickly after initiation and produce heavy rainfall.

After a new cell is triggered, which is labeled cell A (Fig. 16b), it intensifies and produces a cold pool underneath, which merges with the cold pool of earlier cells and pushes the gust front westwards. The gust front subsequently triggers the next cell along the convergence line (cell B) as cell A moves slightly downstream away from the gust front (Fig. 16c). The process can repeat several times, and produce a sequence of convective cells that eventually merge to form a linear MCS. The repeated triggering of new cells upstream of an MCS is commonly referred to as back building, since it occurs on the back side of the MCS. As the cells move slowly along the same line, extreme precipitation can be produced under favorable environmental conditions, as is the current case.

The strong radar echoes that can exceed 50 dBZ of the cells are mostly found below the freezing level or about 4 km height, suggesting that warm rain dominates the precipitation processes. Low echo centroid is often found in extreme precipitation cases during the warm season in China where low-level moisture is plenty. The precipitation efficiency of the convective cells can reach 80%, i.e., 80% of water vapor fluxes into the convective storm is rained out to the ground, which is another important factor of the extreme precipitation. The generally very humid environment is the middle to lower troposphere should have contributed to the high precipitation efficiency.

The effect of cool pool and the associated back building process are further confirmed by a sensitivity experiment in which evaporative cooling within microphysics is turned off. In this case, the quasi-stationary convergence line shifted southward in the absence of the cold pool generated by the earlier rainband, and no new cells are initiated along the convergence line upstream or west of the rainband. The cold pool and associated gust front are essential components of the back-building MCS.

Acknowlegements. This work was supported by the National natural science foundation of China under Grant No. 41730965, the National natural science foundation of China under Grant No. U2242204, the National Key Basic Research and Development Project of China under Grant No. 2013CB430104, the National natural science foundation of China under Grant No. 41175047,. The Key Project of the Joint Funds of Natural Science Foundation of Zhejiang Province under Grant No. LZJMZ23D050003. The first author gratefully acknowledges financial support from the China Scholarship Council for her visit to CAPS, University of Oklahoma.

References

Barthlott, C., and S. Davolio, 2016: Mechanisms initiating heavy precipitation over Italy during HyMeX Special Observation Period 1: a numerical case study using two mesoscale models. *Q. J. Roy. Meteor. Soc.*, 142: 238-258. doi:10.1002/qj.2630

Bluestein, H. B., and M. H. Jain, 1985: Formation of mesoscale lines of precipitation: Severe squall lines in Oklahoma during the spring. *J. Atmos. Sci.*, *42*(16), 1711-1732.

Bresson, E., V. Ducrocq, O. Nuissier, et al., 2012: Idealized numerical simulations of quasi-stationary convective systems over the Northwestern Mediterranean complex terrain. *Q. J. Roy. Meteor. Soc.*, 138(668): 1751-1763. https://doi.org/10.1002/qj.1911

Chen, T. G., and C. Chang, 1980: The Structure and Vorticity Budget of an Early

Summer Monsoon Trough (Mei-Yu) over Southeastern China and Japan. *Mon. Wea. Rev.*, 108, 942–953. https://doi.org/10.1175/1520-0493(1980)108<0942:TSAVBO>2.0.CO;2

Corfidi, S. F., 2003: Cold Pools and MCS Propagation: Forecasting the Motion of Downwind-Developing MCSs. *Wea. Forecasting,* 18, 997–1017. https://doi.org/10.1175/1520-0434(2003)018<0997:CPAMPF>2.0.CO;2

Dahl, N., and M. Xue, 2016: Prediction of the 14 June 2010 Oklahoma City Extreme Precipitation and Flooding Event in a Multiphysics Multi-Initial-Conditions Storm-Scale Ensemble Forecasting System. *Wea. Forecasting,* 31, 1215–1246. https://doi.org/10.1175/WAF-D-15-0116.1

Davolio, S., A. Volonté, A. Manzato, et al., 2016: Mechanisms producing different precipitation patterns over north-eastern Italy: insights from HyMeX-SOP1 and previous events. *Q. J. Roy. Meteor. Soc.*, 142(S1): 188-205. https://doi.org/10.1002/qj.2731

Dawson, D. T., II, M. Xue, J. A. Milbrandt, et al., 2010: Comparison of evaporation and cold pool development between single-moment and multi-moment bulk microphysics schemes in idealized simulations of tornadic thunderstorms. *Mon. Wea. Rev.*, 138, 1152-1171.

Ding, Y., 1992: Summer monsoon rainfalls in China. *Journal of the Meteorological Society of Japan. Ser. II*, *70*(1B), 373-396.

Ding, Y., and J. C. Chan, 2005: The East Asian summer monsoon: an overview. Meteorology and Atmospheric Physics, 89(1-4), 117-142.

Doswell, C. A., H. E. Brooks, and R. A. Maddox, 1996: Flash Flood Forecasting: An Ingredients-Based Methodology. *Wea. Forecasting,* 11, 560–581. https://doi.org/10.1175/1520-0434(1996)011<0560:FFFAIB>2.0.CO;2

Ducrocq, V., O. Nuissier, D. Ricard, et al. 2008: A numerical study of three catastrophic precipitating events over southern France. II: Mesoscale triggering and stationarity factors. *Q. J. Roy. Meteor. Soc.*, 134(630): 131-145. https://doi.org/10.1002/qj.199

Dudhia, J., 1989: Numerical study of convection observed during the winter monsoon experiment usinga mesoscale two-dimensional model. *J. Atmos. Sci.*,46, 3077–3107. doi: 10.1175/1520-0469(1989)046<3077:NSOCOD>2.0.CO;2

Duffourg, F., K. O. Lee, V. Ducrocq, et al., 2018: Role of moisture patterns in the backbuilding formation of HyMeX IOP13 heavy precipitation systems. *Q. J. Roy. Meteor. Soc.*, 144(710): 291-303. https://doi.org/10.1002/qj.3201

Grell, G. A. and D. Devenyi, 2002: A generalized approach to parameterizing convection combining en-semble and data assimilation techniques. *Geophys. Res. Lett.*, 29(14), 1693–1697, doi: 10.1029/2002GL015311

Houston, A. L. and R. B. Wilhelmson, 2007: Observational Analysis of the 27 May 1997 Central Texas Tornadic Event. Part I: Prestorm Environment and Storm Maintenance/Propagation. *Mon. Wea. Rev.,* 135, 701–726. https://doi.org/10.1175/MWR3300.1

Houston, A. L. and R. B. Wilhelmson. 2012: The Impact of Airmass Boundaries on the Propagation of Deep Convection: A Modeling-Based Study in a High-CAPE, Low-Shear Environment. *Mon. Wea. Rev.,* 140, 167–183. https://doi.org/10.1175/MWR-D-10-05033.1

Houze, R. A., B. F. Smull, and P. Dodge, 1990: Mesoscale Organization of Springtime Rainstorms in Oklahoma. *Mon. Wea. Rev.,* 118, 613–654. https://doi.org/10.1175/1520-0493(1990)118<0613:MOOSRI>2.0.CO;2

Houze, R. A., W. Schmid, R. G. Fovell, et al., 1993: Hailstorms in Switzerland: Left Movers, Right Movers, and False Hooks. *Mon. Wea. Rev.,* 121, 3345–3370. https://doi.org/10.1175/1520-00493(1993)121<3345:HISLMR>2.0.CO;2

Huang, H., M. Yang, and C. Sui, 2014: Water Budget and Precipitation Efficiency of Typhoon Morakot (2009). *J. Atmos. Sci.*, 71, 112–129. https://doi.org/10.1175/JAS-D-13-053.1

Huang, Y. J., Y. B. Liu, Y. W. Liu, et al., 2019: Budget analyses of a record-breaking rainfall event in the coastal metropolitan city of Guangzhou, China. *J. Geophys. Res.*, 124(16), 9391–9406. https://doi.org/10.1029/2018jd030229

Janjic, Z. I., 1994: The step-mountain eta coordinate model: Further developments of the convection, viscous sublayer, and turbulence closure schemes. *Mon. Wea. Rev.*, 122(5): 927-945. doi:10.1175/1520-0493(1994)122,0927:TSMECM.2.0.CO;2.

Janjic, Z. I., 1996: The surface layer parameterization in the NCEP Eta Model. Preprints, 11th Conf. on Numerical Weather Prediction, Norfolk, VA, Amer. Meteor. Soc., 354–355.

Jeong, J., D. Lee, and C. Wang, 2016: Impact of the Cold Pool on Mesoscale

Convective System–Produced Extreme Rainfall over Southeastern South Korea: 7 July 2009. *Mon. Wea. Rev.*, 144, 3985–4006. https://doi.org/10.1175/MWR-D-16-0131.1

Klemp, J. P., W. C. Skamarock, and J. Dudhia, 2007: Conservative split-explicit time integration methods for the compressible nonhydrostatic equations. *Mon. Wea. Rev.*, 135, 2897–2913. doi: 10.1175/MWR3440.1

Li, H., Y. Huang, S. Hu, et al., 2021: Roles of terrain, surface roughness, and cold pool outflows in an extreme rainfall event over the coastal region of South China. *J. Geophys. Res.*, 126, e2021JD035556. https://doi.org/10.1029/2021JD035556

Lin, Y., R. L. Deal, and M. S. Kulie, 1998: Mechanisms of Cell Regeneration, Development, and Propagation within a Two-Dimensional Multicell Storm. *J. Atmos. Sci.*, 55, 1867–1886. https://doi.org/10.1175/1520-0469(1998)055<1867:MOCRDA>2.0.CO;2

Liu, R., S. C. Liu, and R. J. Cicerone, et al., 2015: Trends of extreme precipitation in eastern China and their possible causes. *Adv. Atmos. Sci.*, *32*(8), 1027-1037.

Luo, Y., Y. Gong, and D. Zhang, 2014: Initiation and Organizational Modes of an Extreme-Rain-Producing Mesoscale Convective System along a Mei-Yu Front in East China. *Mon. Wea. Rev.*, 142, 203–221. https://doi.org/10.1175/MWR-D-13-00111.1

Maddox, R. A., C. F. Chappell, and L. R. Hoxit, 1979: Synoptic and meso-α scale aspects of flash flood events. *Bull. Amer. Meteor. Soc.*, 115-123.

Merritt, J. H., and F. J. Michael, 1984: On the movement of the heavy precipitation areas of mid-latitude mesoscale convective complexes. *Conference on Weather Forecasting and Analysis, 10 th, Clearwater Beach, FL.*

Mlawer, E. J., S. J. Taubman, P. D. Brown, et al., 1997: Radiative transfer for inhomogeneous atmospheres: RRTM, a validated correlated-k model for the longwave. *J. Geophys. Res., 102*(D14), 16663-16682.

Moore, B. J., P. J. Neiman, F. M. Ralph, et al., 2012: Physical Processes Associated with Heavy Flooding Rainfall in Nashville, Tennessee, and Vicinity during 1–2 May 2010: The Role of an Atmospheric River and Mesoscale Convective Systems. *Mon. Wea. Rev.,* 140, 358–378. https://doi.org/10.1175/MWR-D-11-00126.1

Moore, J. T., F. H. Glass, C.E. Graves, et al., 2003: The Environment of Warm-Season Elevated Thunderstorms Associated with Heavy Rainfall over the Central United States. *Wea. Forecasting,* 18, 861–878. https://doi.org/10.1175/1520-0434(2003)018<0861:TEOWET>2.0.CO;2

Parker, M. D., and R. H. Johnson, 2000: Organizational Modes of Midlatitude Mesoscale Convective Systems. *Mon. Wea. Rev.,* 128, 3413–3436. https://doi.org/10.1175/1520-0493(2001)129<3413:OMOMMC>2.0.CO;2

Peters, J. M. and R. S. Schumacher, 2016: Dynamics Governing a Simulated Mesoscale Convective System with a Training Convective Line. *J. Atmos. Sci.*, 73, 2643–2664. https://doi.org/10.1175/JAS-D-15-0199.1

Schumacher, R. S. and R. H. Johnson, 2009: Quasi-Stationary, Extreme-Rain-

Producing Convective Systems Associated with Midlevel Cyclonic Circulations. *Wea. Forecasting*, 24, 555–574. https://doi.org/10.1175/2008WAF2222173.1

Schumacher, R. S. and R. H. Johnson, 2005: Organization and Environmental Properties of Extreme-Rain-Producing Mesoscale Convective Systems. *Mon. Wea. Rev.,* 133,961–976. https://doi.org/10.1175/MWR2899.1

Skamarock, W. C., J. B. Klemp, J. Dudhia, et al., 2007: A description of the advanced research WRF version 2. Tech. rep., NCAR Tech. Note NCAR/TN-468 STR, 100pp

Sui, C., X. Li, and M. Yang, 2007: On the Definition of Precipitation Efficiency. *J. Atmos. Sci.*, 64, 4506–4513. https://doi.org/10.1175/2007JAS2332.1

Sun, J., 2005: Initialization and Numerical Forecasting of a Supercell Storm Observed during STEPS. *Mon. Wea. Rev.*, 133, 793–813. https://doi.org/10.1175/MWR2887.1

Tao, S. and Y. Ding, 1981: Observational Evidence of the Influence of the Qinghai-Xizang (Tibet) Plateau on the Occurrence of Heavy Rain and Severe Convective Storms in China. *Bull. Amer. Meteor. Soc.,* 62, 23–30. https://doi.org/10.1175/1520-0477(1981)062<0023:OEOTIO>2.0.CO;2

Thompson, G., P. R. Field, W. D. Hall, et al., 2006: A new bulk microphysical parameterization for WRF (& MM5) //Proceedings of the 7th Weather Research and Forecasting Model Workshop. 1-11.

Thompson, G., P. R. Field, R. M. Rasmussen, et al., 2008: Explicit forecasts of winter precipitation using an improved bulk microphysics scheme. Part II:

Implementation of a new snow parameterization. *Mon. Wea. Rev*, 136(12): 5095-5115. doi: 10.1175/2008MWR2387.1

Thompson, G., R. M. Rasmussen, and K. Manning, 2004: Explicit forecasts of winter precipitation using an improved bulk microphysics scheme. Part I: Description and sensitivity analysis. *Mon. Wea. Rev.,* 132(2): 519-542. doi: 10.1175/1520-0493(2004)132<0519:EFOWPU>2.0.CO;2

Wang, H., Y. Luo, and B. J. Jou, 2014: Initiation, maintenance, and properties of convection in an extreme rainfall event during SCMREX: Observational analysis. *J. Geophys. Res.*, 119(23). https://doi.org/10.1002/2014JD022339

Wang, C., B.-K. Chiou, G. T.-J. Chen, et al., 2016: A numerical study of back-building process in a quasi-stationary rainband with extreme rainfall over northern Taiwan during 11-12 June 2012. *Atmos. Chem. Phys.*, 16(18), 12359-12382. doi:http://dx.doi.org/10.5194/acp-16-12359-2016

Wang, Q., Y. Zhang, K. Zhu, et al. 2021: A Case Study of the Initiation of Parallel Convective Lines Back-Building from the South Side of a Mei-yu Front over Complex Terrain. *Adv. Atmos. Sci.*, 38(5):20.

Weisman, M.L., C. Evans, and L. Bosart., 2013: The 8 May 2009 Superderecho: Analysis of a Real-Time Explicit Convective Forecast. *Wea. Forecasting,* 28, 863–892, https://doi.org/10.1175/WAF-D-12-00023.1

Xu, X., M. Xue, and Y. Wang. 2015: The genesis of mesovortices within a real-data simulation of a bow echo system. *J. Atmos. Sci.*, 72(5): 1963-1986. doi: 10.1175/JAS-D-14-0209.1

Xu, W., E. J. Zipser, Y. Chen. et al., 2012: An Orography-Associated Extreme Rainfall Event during TiMREX: Initiation, Storm Evolution, and Maintenance. *Mon. Wea. Rev.,* 140, 2555–2574. https://doi.org/10.1175/MWR-D-11-00208.1

Zhai, G., H. Zhang, H. Shen, et al., 2015: Role of a meso-γ vortex in Meiyu torrential rainfall over the Hangzhou Bay, China: An observational study. *J. Meteorol. Res.*, *29*(6), 966-980.

Zheng, Y., M. Xue, B. Li, et al., 2016: Spatial characteristics of extreme rainfall over China with hourly through 24-hour accumulation periods based on national-level hourly rain gauge data. *Adv. Atmos. Sci.*, *33*(11), 1218-1232.

Zhou, X., Z. Bai, and Y. Yang, 2017: Linking trends in urban extreme rainfall to urban flooding in China. *Int. J. Climatol.*, *37*(13), 4586-4593.

Figure captions:

Figure 1: (a) Distribution of the 4-h accumulated rainfall (shaded, mm) from 0700 - 1100 UTC 24 June, 2013. The station names are abbreviated in Tongxiang (TX), Linping (LP), Xingqiao (XQ), and Gongchenqiao (GCQ). JiangXing and Hangzhou are the names of two cities in Zhejiang Province. The gray lines denote the two rainbands. (b) Temporal variation of 10-min accumulated rainfall (mm) at four stations: TX (red line), LP (black line), XQ (green line), and GCQ (blue line), respectively, during 0700 – 1200 UTC 24 June, 2013.

Figure 2: Composite radar reflectivity (dBZ) observed by Hangzhou and Ningbo radars. Convective cells are indicated by C1, C2, C3 from 0700 to 1200 UTC 24 June, 2013 .

Figure 3: Environmental features based on ECMWF ERA-Interim at 0600 UTC 24 June 2013.The geopotential height (black solid lines, contour interval of 20 gpm), equivalent potential temperature (shaded), and the winds (a full barb is 4 m s-1) at (a) 1000-hPa, (b) 850-hPa. (c) 200-hPa geopotential height (black solid lines, contour interval of 20 gpm), horizontal divergence (shaded), and the winds (a full barb is 4 m s-1). The distribution of a surface stationary front indicates the location of the Mei-Yu front. The dashed blue rectangle denotes the position of shear line. Letters H, L, W and C denote the centers of a high and low pressure system, and the warm and cold air, respectively.

Figure 4: Objective analyses of 2-m temperature (shaded, °C), 10-minutes accumulated rainfall (blue contours at 1×2N mm, where N = 0, 1, 2, 3,…), and streamlines of 10-m winds observed by automated weather stations at the times shown (in UTC) of 24 June, 2013.

Figure 5: The four nested domains for numerical simulations. Domains d01, d02 and d03 labeled have 27, 9, and 3 km grid spacing, respectively. The innermost black rectangle is for the 1 km grid spacing domain d04.

Figure 6: The distribution of 4-h accumulated rainfall (shaded, mm) during the period of 0500-0900 UTC from the finest-resolution (1 km) domain. The gray lines denote the two rainbands. The pink rectangle indicates the region for calculation of area-averaged hourly rainfall.

Figure 7: Same as Figure 2, but for the control simulation on the 1 km grid. The simulated convective cells denote by A, B, C, D. The black dashed line denotes the gust front, who was simply defined by the wind filed. The black rectangle box in Fig. 7d denotes the region used to calculate precipitation efficiency. The black line in Fig. 7d denotes the location of the cross-section shown in Figs. 10 and 11.

Figure 8: Surface potential temperature perturbation of -1 K (black contours, indicating the cold pool edge), and streamlines at 0540 UTC. The shading in (a) shows CAPE (J kg -1), and in (b) water vapor mixing ratio (g kg -1) at 0540 UTC. The purple contours are 45 dBZ composite radar reflectivity at 0720 UTC. The blue star in Fig. 8a indicates the location of extracted sounding shown in Fig. 9.

Figure 9: Sounding extracted from the simulation at (a) 0440UTC and (b) 0540 UTC, at the location of blue star in Fig. 8a.

Figure 10: Vertical cross sections along the line in Fig. 7d of simulated radar reflectivity (shaded, dBZ), equivalent potential temperature θ_e (black contours at 4 K intervals), 0°C temperature (purple contours), and in-plane wind vectors with vertical velocity

amplified by a factor of 3. The upward arrows below the panels denote the location of gust front.

Figure 11: Vertical cross sections along the line in Fig. 7d of potential temperature perturbation (shaded, K), cloud water (contoured in green at 0.3, 0.5, 1 g kg^{-1}), horizontal divergence (contoured in purple starting at -5 $\times 10^{-4}\,s^{-1}$, at intervals of 5 $\times 10^{-4}\,s^{-1}$), 20 dBZ composite radar reflectivity (gray contours), LFC (white line, m), and in-plane wind vectors with vertical velocity amplified by a factor of 3.

Figure 12: (a) Time series of precipitation efficiency PE and (b) the time-height plot of lateral water vapor flux ($\times 10^{-6}$ kg s^{-1}) from 0540 to 0740 UTC.

Figure 13: Simulated composite radar reflectivity (shaded, dBZ) and the streamlines of 10-m winds of experiment NOEVAP at different times of simulation.

Figure 14: 2-m temperature (shaded, °C), 10-minutes accumulated rainfall (purple contours at 1×2^{N}mm, where N = 0, 1, 2, 3,…), and streamlines of 10-m winds from the control experiment (upper panels) and experiment NOEVAP (lower panels) at the times (in UTC) labeled in the figure. The red triangle denotes the location of cell A's initiation.

Figure 15. Time series of area-averaged 10-min rainfall over the pink rectangle in Fig. 6 for control run (black) and NOEVAP run (red) from 0500 UTC and 0900 UTC.

Figure 16: Conceptual model illustrating the back-building processes in the extreme rainfall event. The blue ellipse indicates the surface cold pool. The dark gray dashed lines indicate the mesoscale convergence boundary. The blue cold front symbols indicate the gust front on the southwest side of the cold pool. The light gray ellipses indicate the convergence region forced by the gust front and mesoscale convergence

boundary. Panels (a), (b) and (c) illustrate different stages of the back-building MCS.

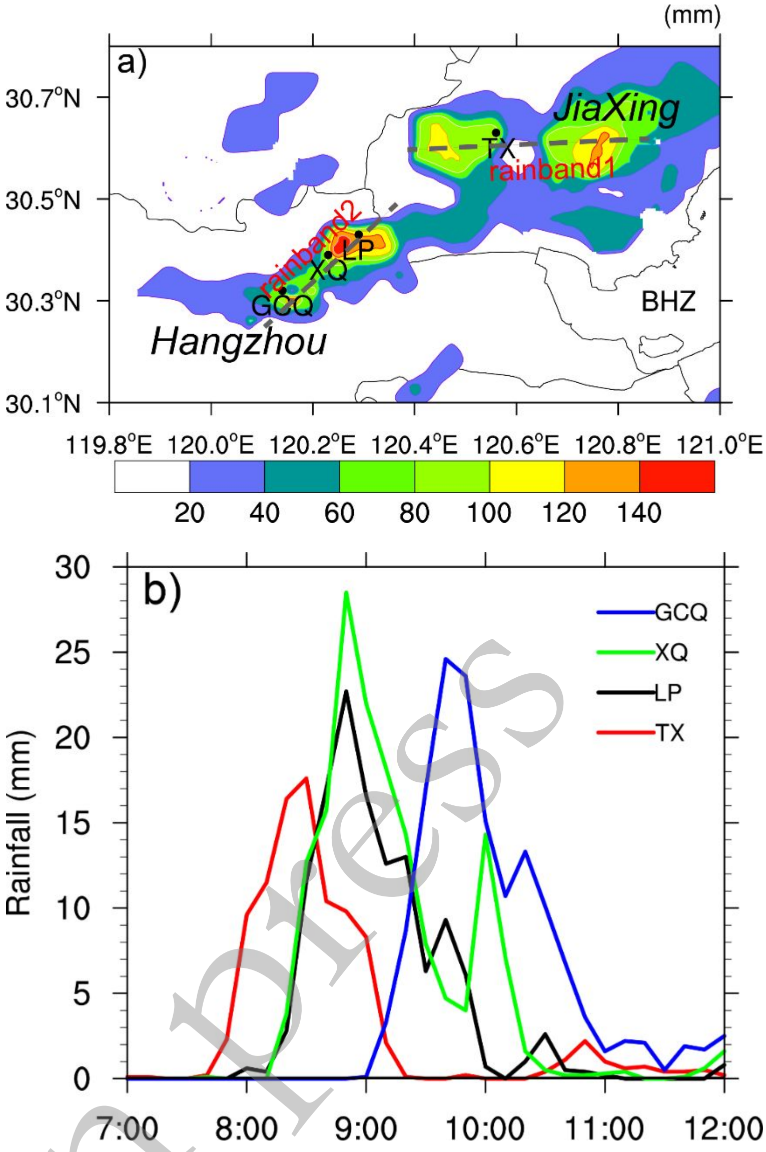

Figure 1: (a) Distribution of the 4-h accumulated rainfall (shaded, mm) from 0700 - 1100 UTC 24 June, 2013. The station names are abbreviated in Tongxiang (TX), Linping (LP), Xingqiao (XQ), and Gongchenqiao (GCQ). JiangXing and Hangzhou are the names of two cities in Zhejiang Province. The gray lines denote the two rainbands. (b) Temporal variation of 10-min accumulated rainfall (mm) at four stations: TX (red line), LP (black line), XQ (green line), and GCQ (blue line), respectively, during 0700 – 1200 UTC 24 June, 2013.

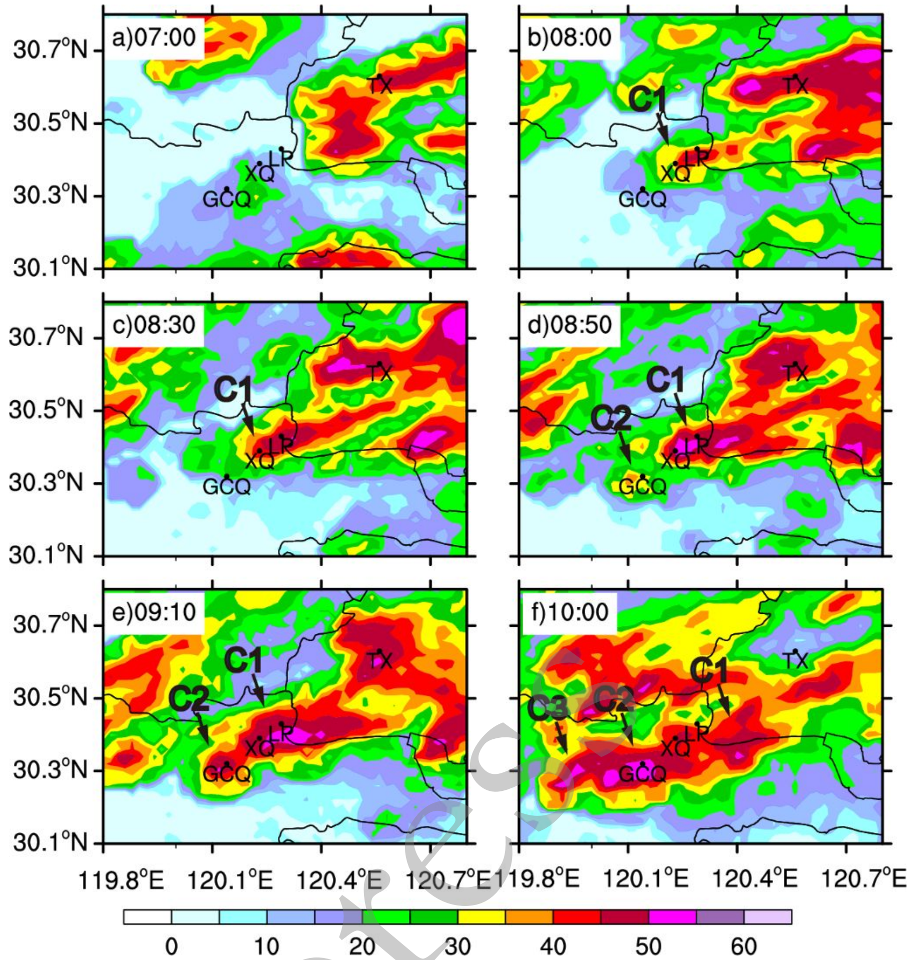

Figure 2: Composite radar reflectivity (dBZ) observed by Hangzhou and Ningbo radars.

Convective cells are indicated by C1, C2, C3 from 0700 to1200 UTC 24 June, 2013.

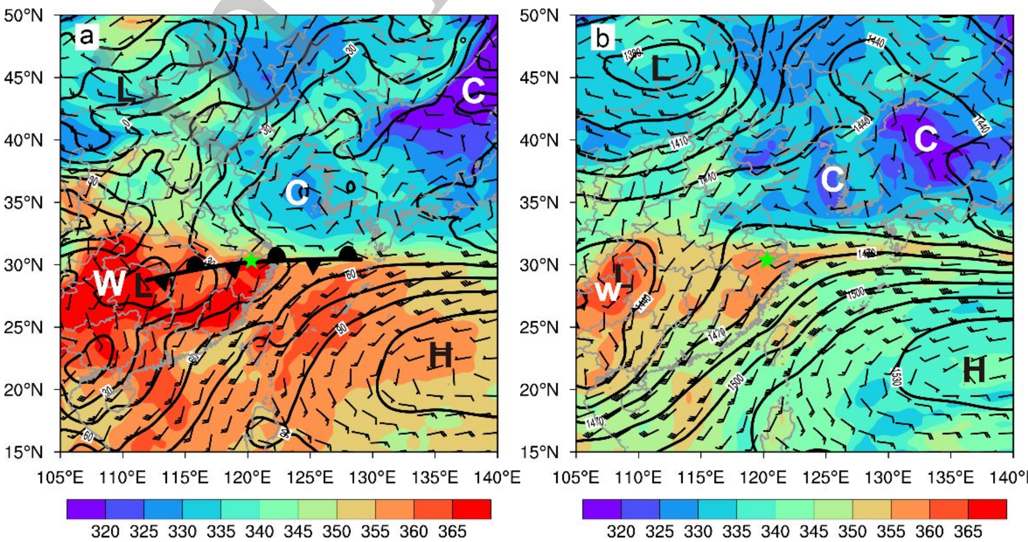

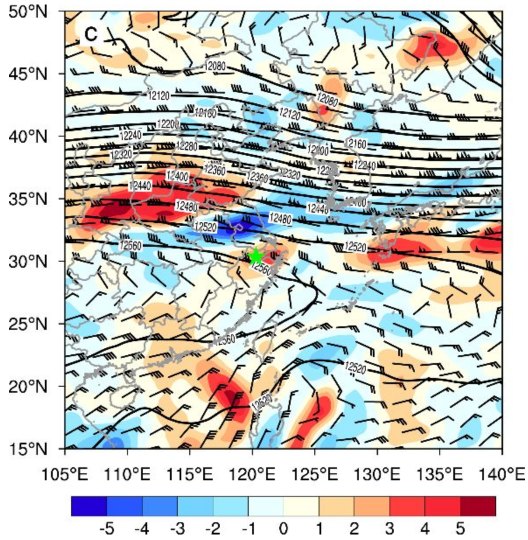

Figure 3: Environmental features based on ECMWF ERA-Interim at 0600 UTC 24 June 2013.The geopotential height (black solid lines, contour interval of 20 gpm), equivalent potential temperature (shaded), and the winds (a full barb is 4 m s^{-1}) at (a) 1000-hPa, (b) 850-hPa. (c) 200-hPa geopotential height (black solid lines, contour interval of 20 gpm), horizontal divergence (shaded), and the winds (a full barb is 4 m s^{-1}). The distribution of a surface stationary front indicates the location of the Mei-Yu front. The dashed blue rectangle denotes the position of shear line. Letters H, L, W and C denote the centers of a high and low pressure system, and the warm and cold air, respectively.

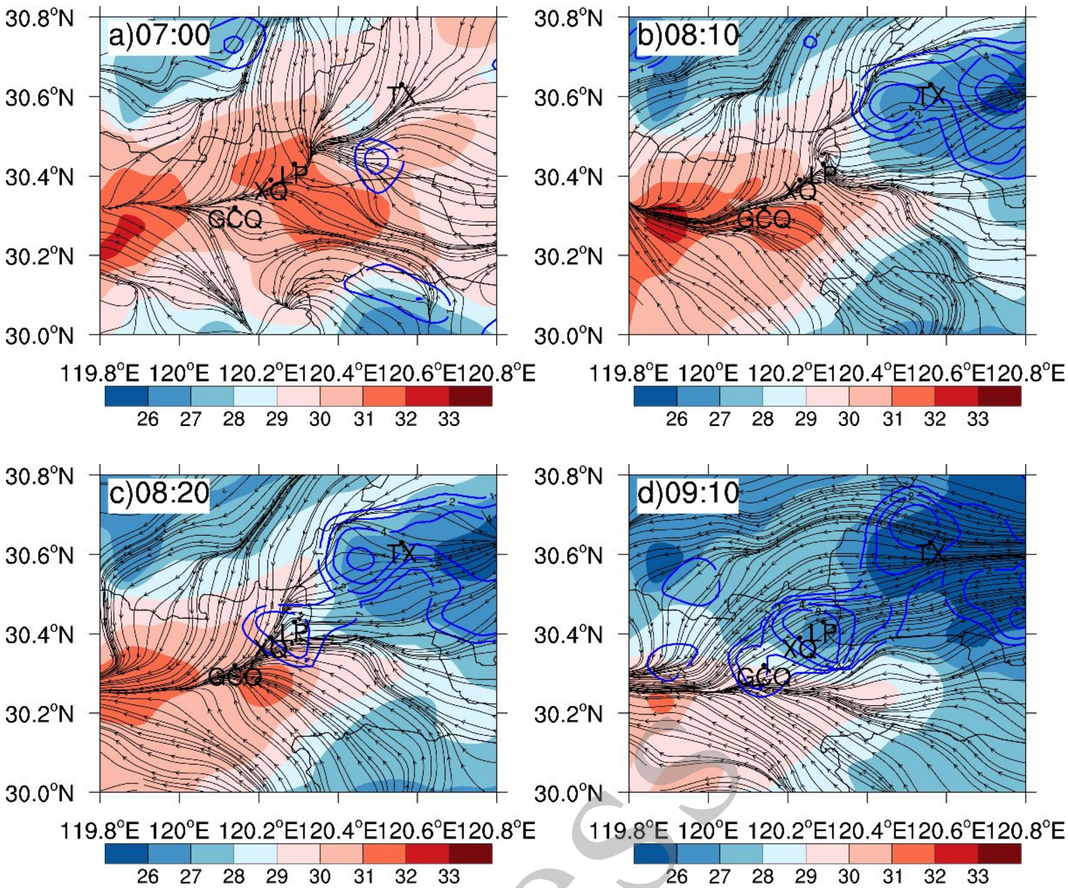

Figure 4: Objective analyses of 2-m temperature (shaded, ℃), 10-minutes accumulated rainfall (blue contours at 1×2^{N} mm, where $N = 0, 1, 2, 3, \ldots$), and streamlines of 10-m winds observed by automated weather stations at the times shown (in UTC) of 24 June, 2013.

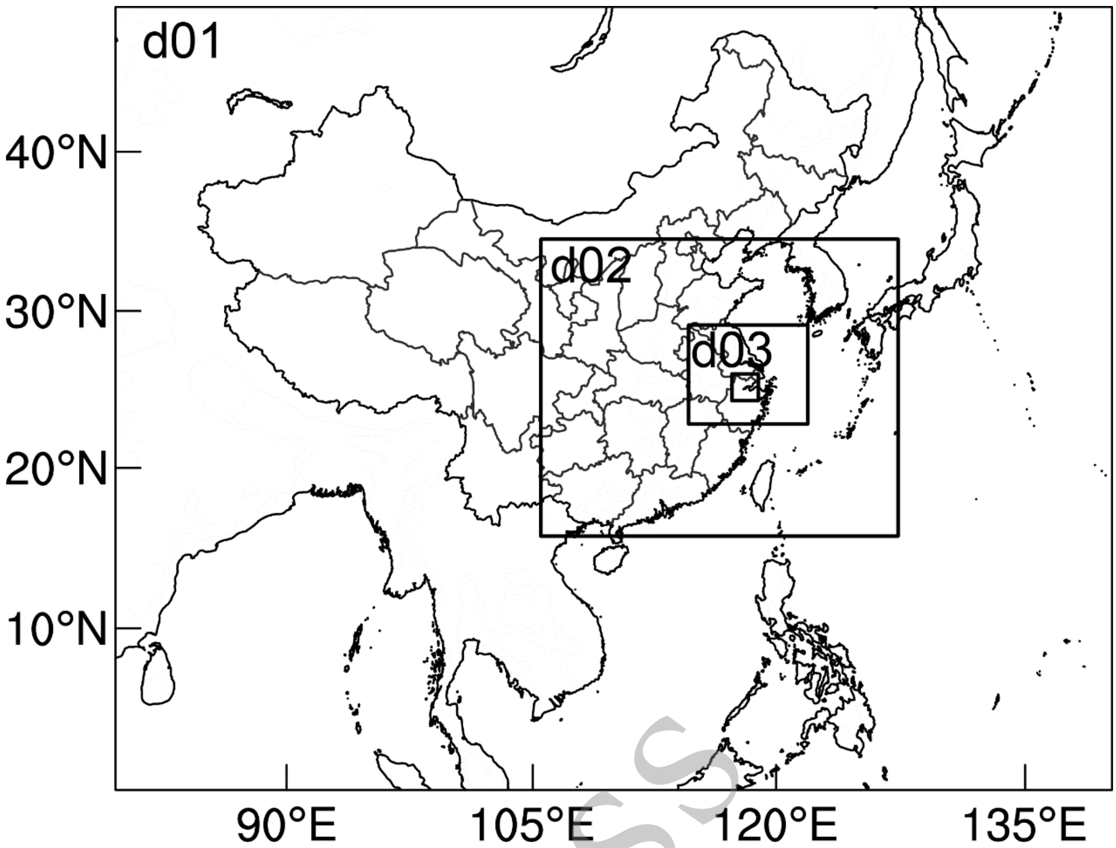

Figure 5: The four nested domains for numerical simulations. Domains d01, d02 and d03 labeled have 27, 9, and 3 km grid spacing, respectively. The innermost black rectangle is for the 1 km grid spacing domain d04.

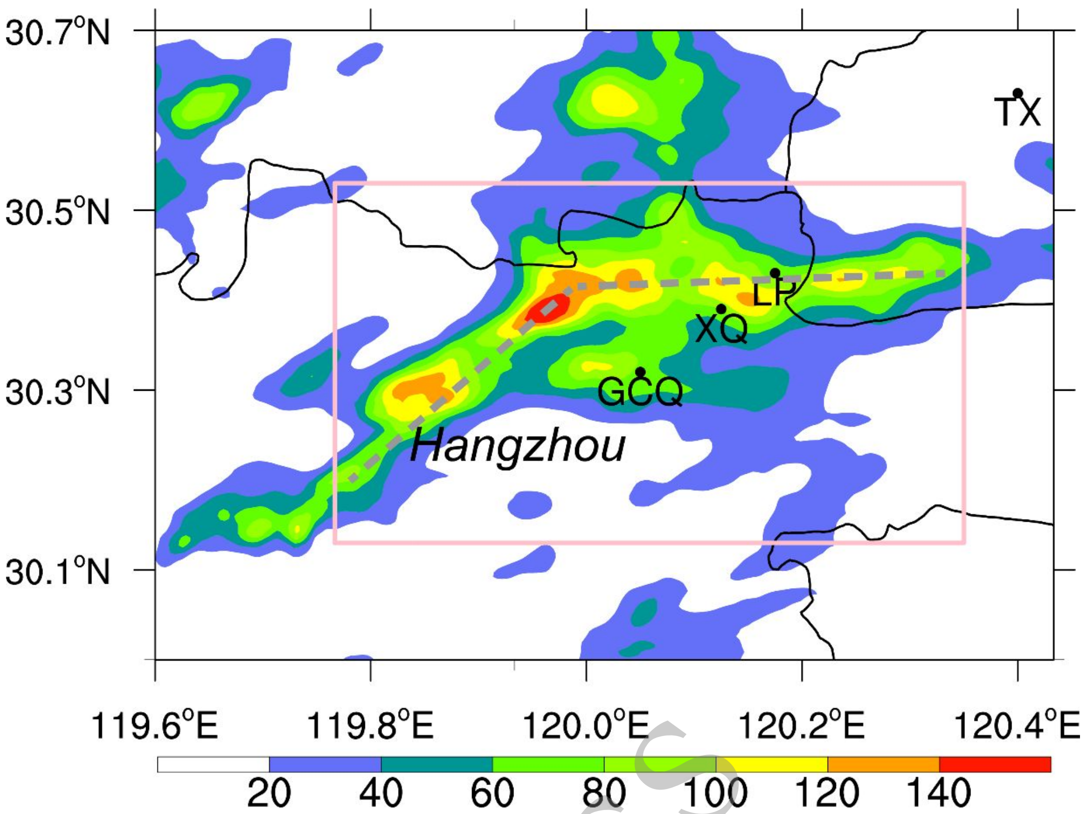

Figure 6: The distribution of 4-h accumulated rainfall (shaded, mm) during the period of 0500-0900 UTC from the finest-resolution (1 km) domain. The gray lines denote the two rainbands. The pink rectangle indicates the region for calculation of area-averaged hourly rainfall.

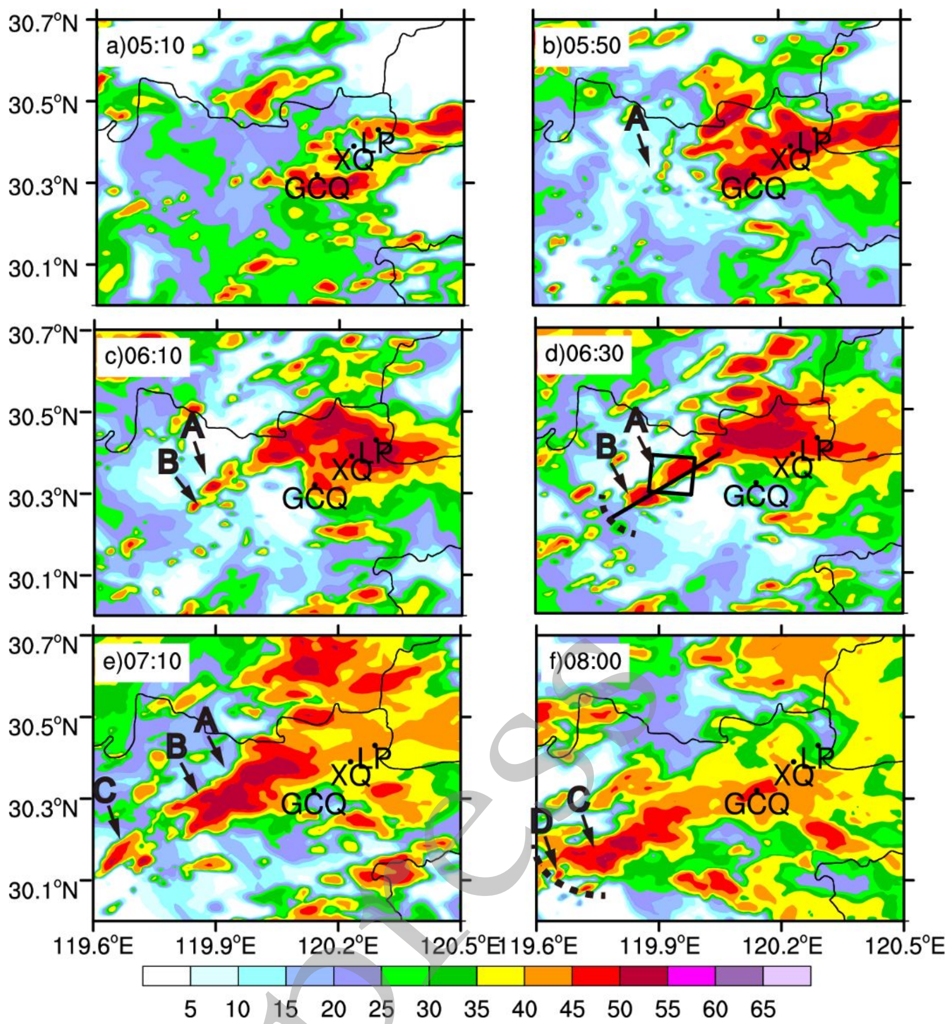

Figure 7: Same as Figure 2, but for the control simulation on the 1 km grid. The simulated convective cells denote by A, B, C, D. The black dashed line denotes the gust front, who was simply defined by the wind filed. The black rectangle box in Fig. 7d denotes the region used to calculate precipitation efficiency. The black line in Fig. 7d denotes the location of the cross-section shown in Figs. 10 and 11.

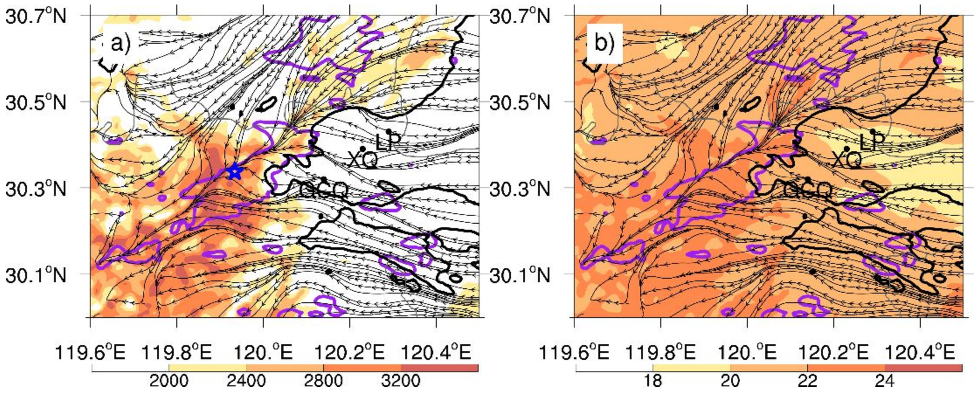

Figure 8: Surface potential temperature perturbation of -1 K (black contours, indicating the cold pool edge), and streamlines at 0540 UTC. The shading in (a) shows CAPE (J kg $^{-1}$), and in (b) water vapor mixing ratio (g kg $^{-1}$) at 0540 UTC. The purple contours are 45 dBZ composite radar reflectivity at 0720 UTC. The blue star in Fig. 8a indicates the location of extracted sounding shown in Fig. 9.

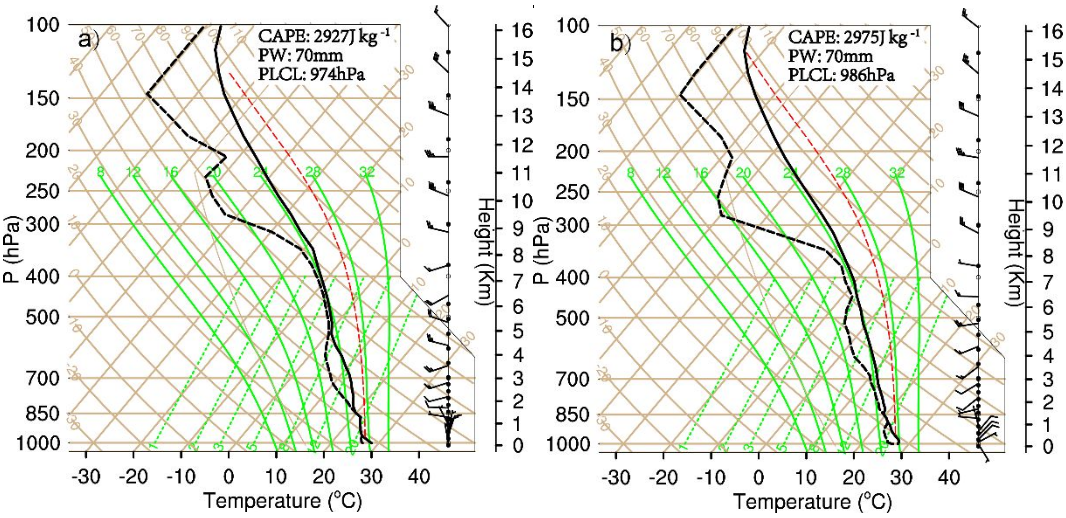

Figure 9: Sounding extracted from the simulation at (a) 0440UTC and (b) 0540 UTC, at the location of blue star in Fig. 8a.

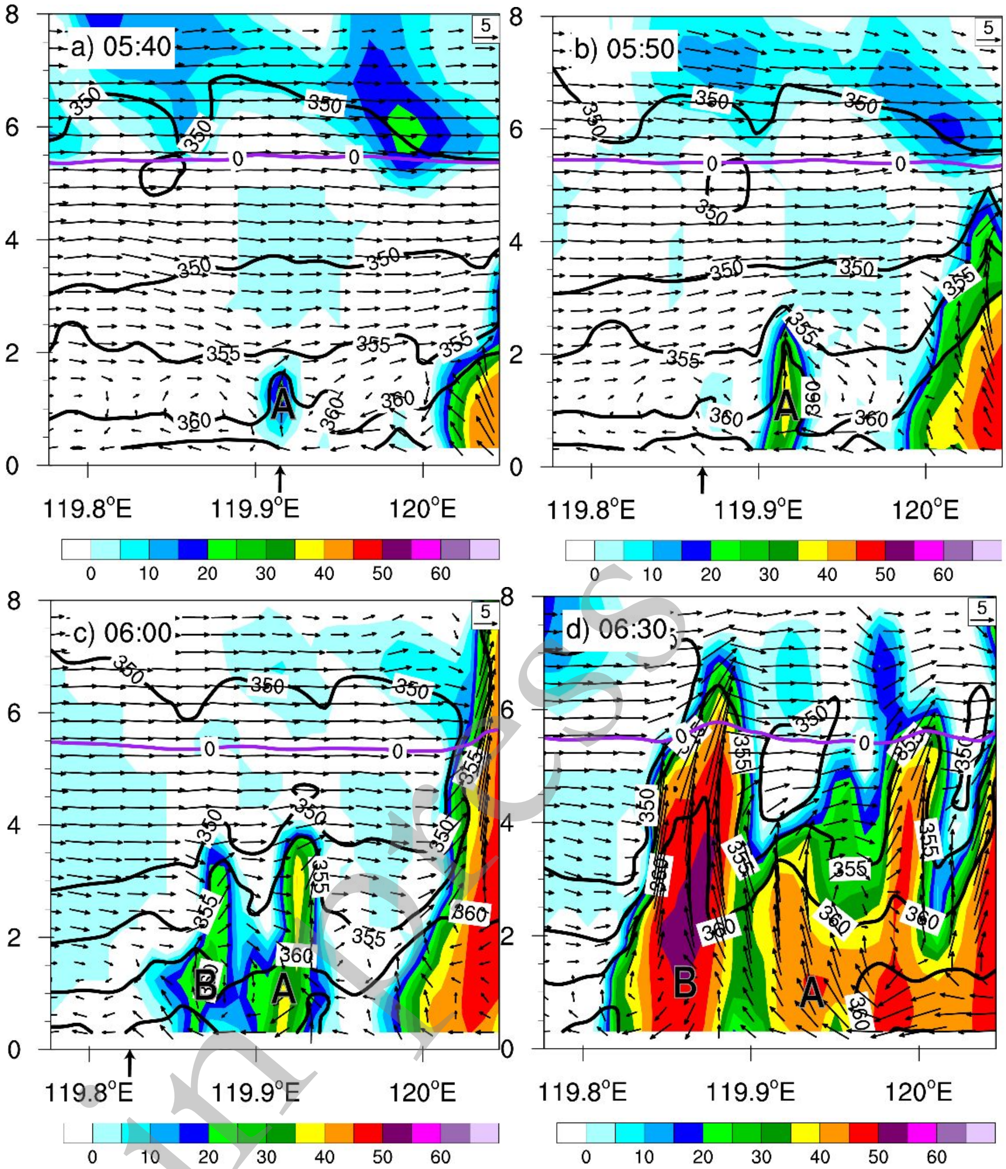

Figure 10: Vertical cross sections along the line in Fig. 7d of simulated radar reflectivity (shaded, dBZ), equivalent potential temperature θ_e (black contours at 4 K intervals), 0℃ temperature (purple contours), and in-plane wind vectors with vertical velocity amplified by a factor of 3. The upward arrows below the panels denote the location of gust front.

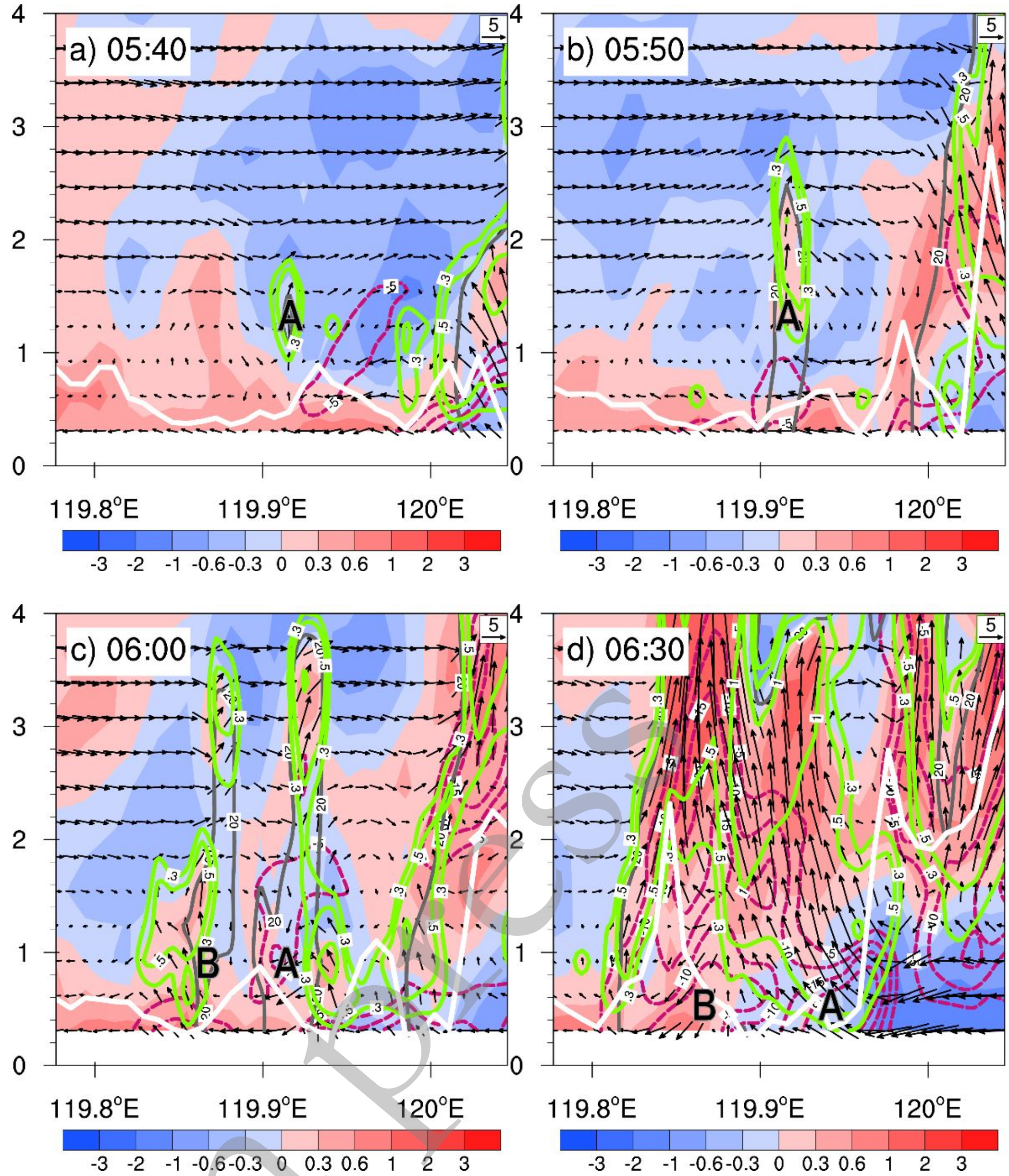

Figure 11: Vertical cross sections along the line in Fig. 7d of potential temperature perturbation (shaded, K), cloud water (contoured in green at 0.3, 0.5, 1 g kg^{-1}), horizontal divergence (contoured in purple starting at -5 $\times 10^{-4}\,s^{-1}$, at intervals of 5 $\times 10^{-4}\,s^{-1}$), 20 dBZ composite radar reflectivity (gray contours), LFC (white line, m), and in-plane wind vectors with vertical velocity amplified by a factor of 3.

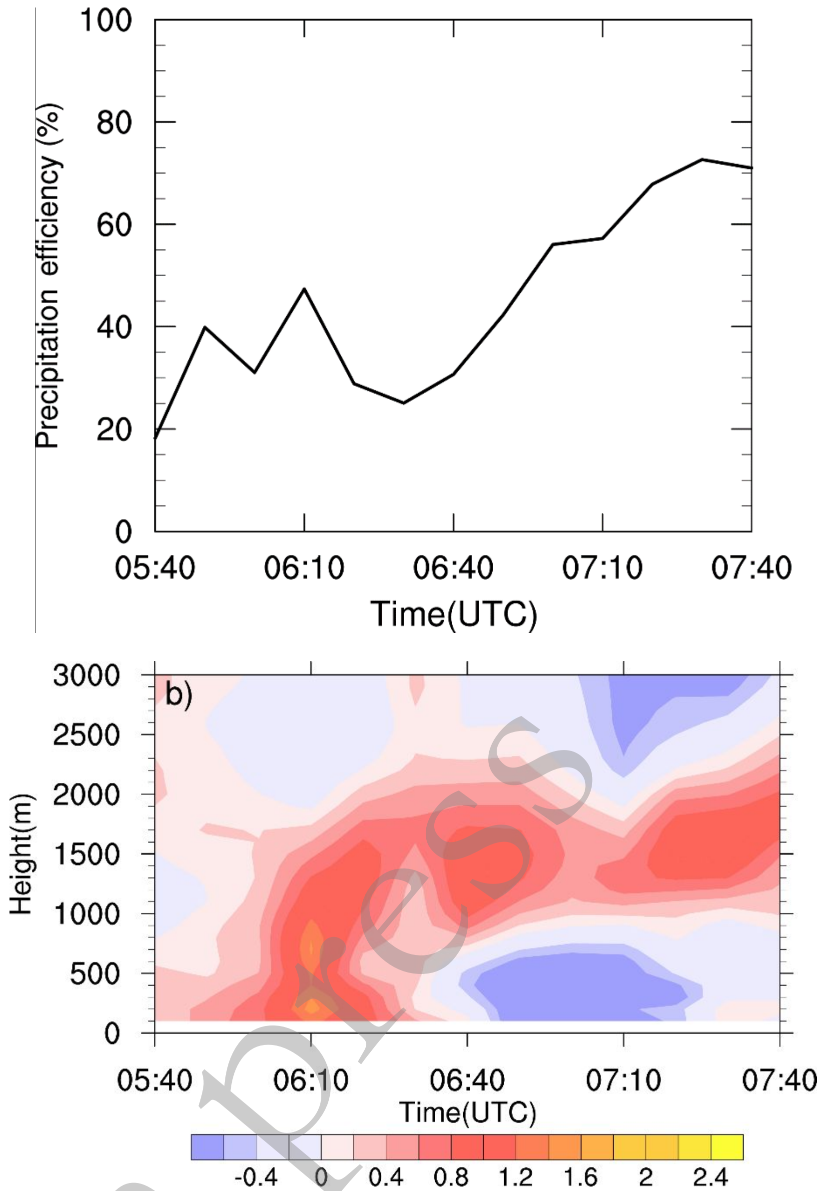

Figure 12: (a) Time series of precipitation efficiency PE and (b) the time-height plot of lateral water vapor flux ($\times 10^{-6}$ kg s^{-1}) from 0540 to 0740 UTC.

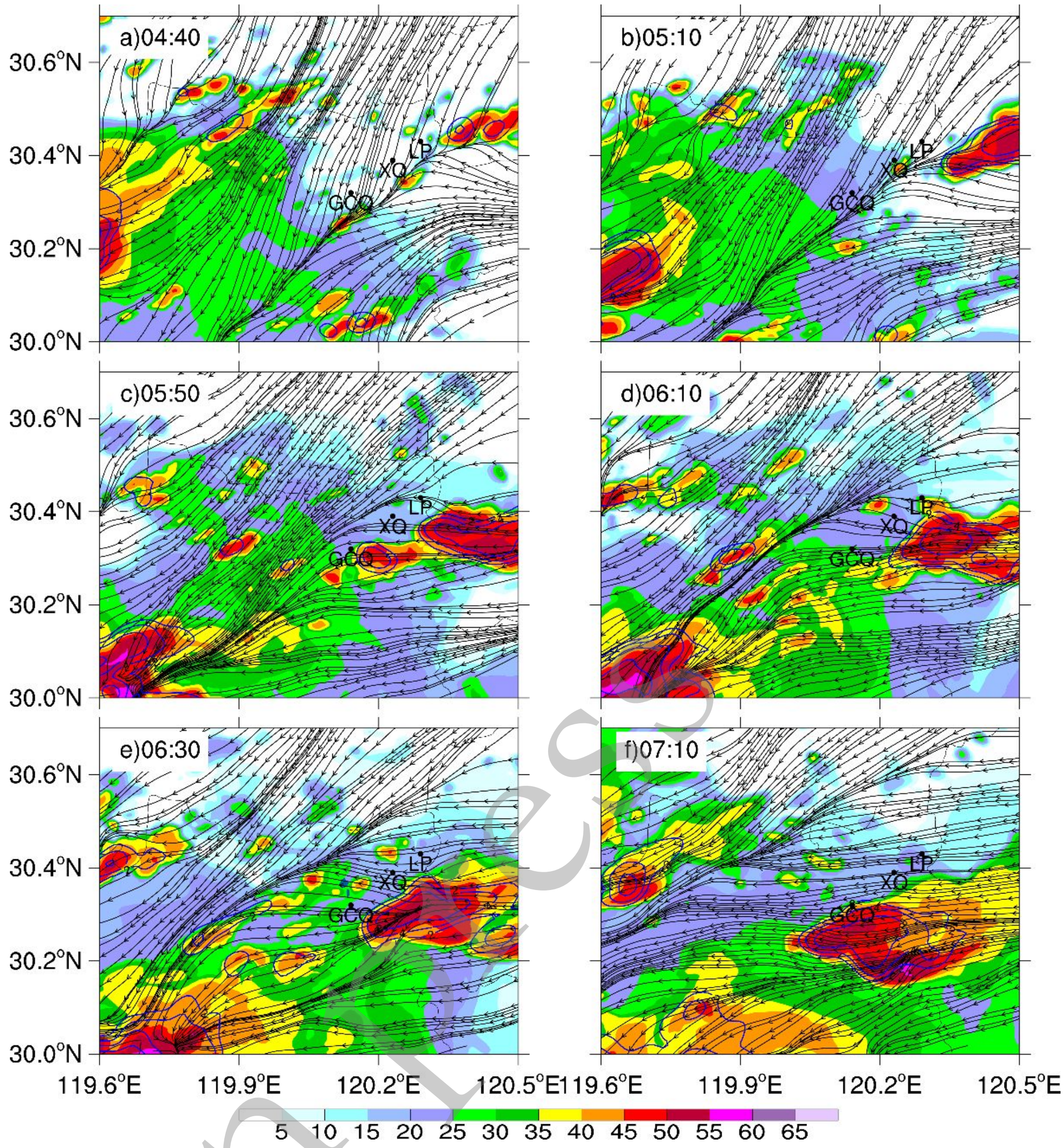

Figure 13: Simulated composite radar reflectivity (shaded, dBZ) and the streamlines of 10-m winds of experiment NOEVAP at different times of simulation.

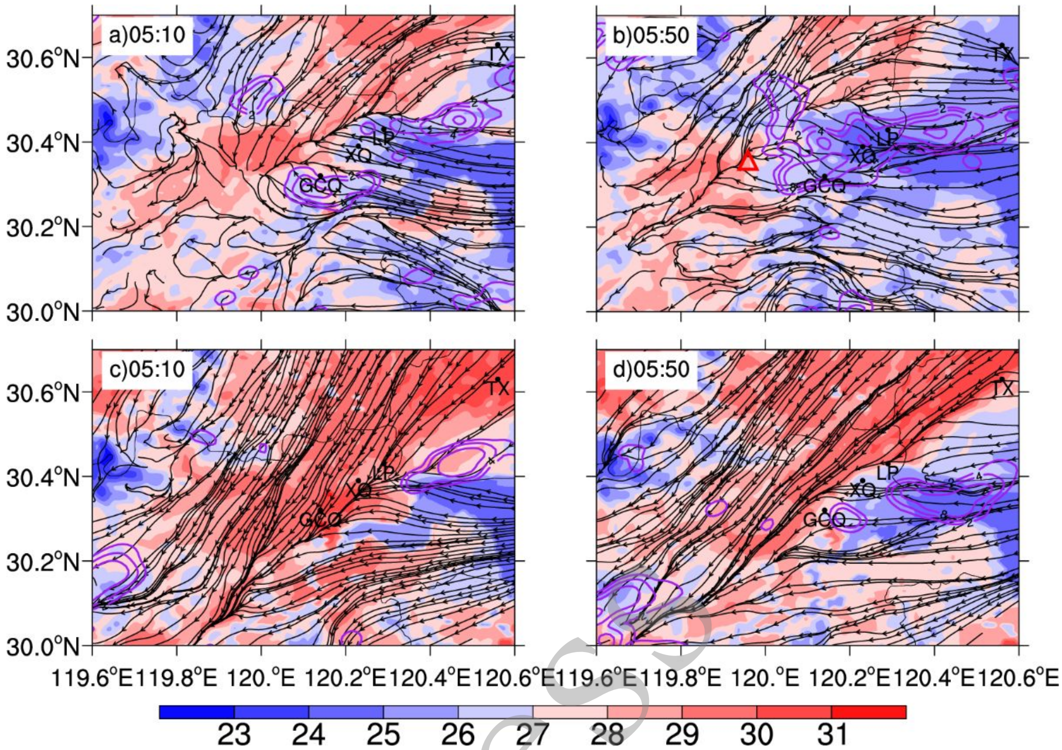

Figure 14: 2-m temperature (shaded, °C), 10-minutes accumulated rainfall (purple contours at 1×2^{N}mm, where N = 0, 1, 2, 3, …), and streamlines of 10-m winds from the control experiment (upper panels) and experiment NOEVAP (lower panels) at the times (in UTC) labeled in the figure. The red trianglein (b) denotes the location of cell A's initiation.

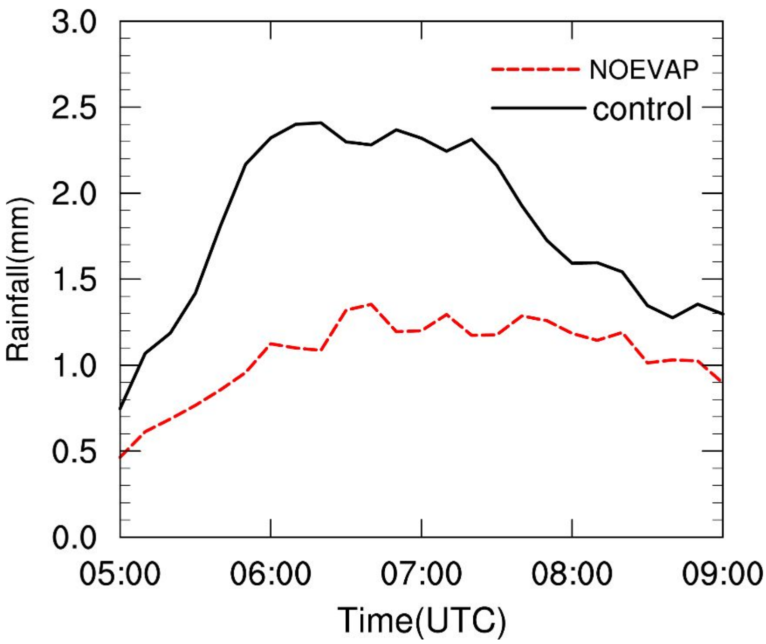

Figure 15. Time series of area-averaged 10-min rainfall over the pink rectangle in Fig. 6 for control run (black) and NOEVAP run (red) from 0500 UTC and 0900 UTC.

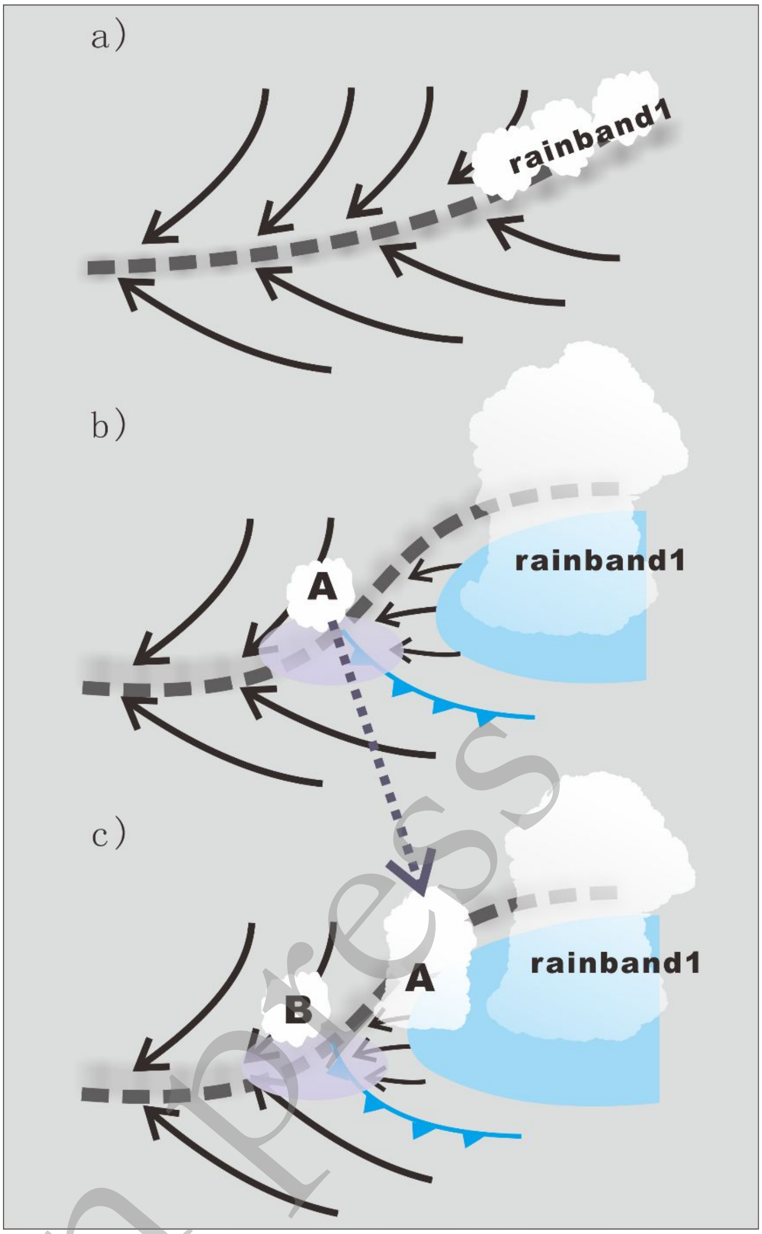

Figure 16: Conceptual model illustrating the back-building processes in the extreme rainfall event. The blue ellipse indicates the surface cold pool. The dark gray dashed lines indicate the mesoscale convergence boundary. The blue cold front symbols indicate the gust front on the southwest side of the cold pool. The light gray ellipses indicate the convergence region forced by the gust front and mesoscale convergence boundary. Panels (a), (b) and (c) illustrate different stages of the back-building MCS.